

Article

Computational Performance of Disparate Lattice Boltzmann Scenarios under Unsteady Thermal Convection Flow and Heat Transfer Simulation

Aditya Dewanto Hartono ^{1,*}, Kyuro Sasaki ^{1,2}, Yuichi Sugai ¹ and Ronald Nguele ¹

¹ Resources Production and Safety Engineering (REPS) Laboratory, Department of Earth Resources Engineering, Kyushu University, Fukuoka 812-0395, Japan; krsasaki@mine.kyushu-u.ac.jp (K.S.); sugai@mine.kyushu-u.ac.jp (Y.S.); nguele@mine.kyushu-u.ac.jp (R.N.)

² Institute for Future Engineering (IFENG), 2-6-11 Fukagawa Koto-ku, Tokyo 135-8473, Japan

* Correspondence: adityadewanto@gmail.com

Abstract: The present work highlights the capacity of disparate lattice Boltzmann strategies in simulating natural convection and heat transfer phenomena during the unsteady period of the flow. Within the framework of Bhatnagar-Gross-Krook collision operator, diverse lattice Boltzmann schemes emerged from two different embodiments of discrete Boltzmann expression and three distinct forcing models. Subsequently, computational performance of disparate lattice Boltzmann strategies was tested upon two different thermo-hydrodynamics configurations, namely the natural convection in a differentially-heated cavity and the Rayleigh-Bénard convection. For the purposes of exhibition and validation, the steady-state conditions of both physical systems were compared with the established numerical results from the classical computational techniques. Excellent agreements were observed for both thermo-hydrodynamics cases. Numerical results of both physical systems demonstrate the existence of considerable discrepancy in the computational characteristics of different lattice Boltzmann strategies during the unsteady period of the simulation. The corresponding disparity diminished gradually as the simulation proceeded towards a steady-state condition, where the computational profiles became almost equivalent. Variation in the discrete lattice Boltzmann expressions was identified as the primary factor that engenders the prevailed heterogeneity in the computational behaviour. Meanwhile, the contribution of distinct forcing models to the emergence of such diversity was found to be inconsequential. The findings of the present study contribute to the ventures to alleviate contemporary issues regarding proper selection of lattice Boltzmann schemes in modelling fluid flow and heat transfer phenomena.

Keywords: lattice Boltzmann method; natural convection modelling; differentially-heated cavity; Rayleigh-Bénard convection; discretization order; forcing models; computational performance



Citation: Hartono, A.D.; Sasaki, K.; Sugai, Y.; Nguele, R. Computational Performance of Disparate Lattice Boltzmann Scenarios under Unsteady Thermal Convection Flow and Heat Transfer Simulation. *Computation* **2021**, *9*, 65. <https://doi.org/10.3390/computation9060065>

Academic Editor: Andrea Montessori

Received: 5 April 2021

Accepted: 27 May 2021

Published: 31 May 2021

Publisher's Note: MDPI stays neutral with regard to jurisdictional claims in published maps and institutional affiliations.



Copyright: © 2021 by the authors. Licensee MDPI, Basel, Switzerland. This article is an open access article distributed under the terms and conditions of the Creative Commons Attribution (CC BY) license (<https://creativecommons.org/licenses/by/4.0/>).

1. Introduction

The Lattice Boltzmann Method (LBM) has raised considerable interest amongst the community of computational fluid dynamics (CFD) due to its efficacy in handling multi-tude fluid flow problems. Relying on the statistical mechanics, LBM regards the flowing materials through the collective behaviour of the accompanying molecules [1,2]. It differs from traditional CFD methods in sense that it solves the representative Boltzmann expression of the flowing substances rather than directly handling the corresponding hydrodynamics equations in their operations. Because of this unique feature, modelling a flow problem using LBM has several advantages, including a clear algorithm [3], straightforward treatment of boundary conditions [4], and innate feasibility for parallel computing architecture [5]. As a promising numerical tool, LBM is currently a vibrant research topic in the discipline of CFD.

As far as modelling the flow problem using LBM is concerned, two properties are routinely considered: (a) the discrete lattice Boltzmann expressions, and (b) the discrete

forcing schemes. The former parameter has been extensively discussed in the literature. Ubertini et al. [6] investigated three distinct models of discrete lattice Boltzmann expression for hydrodynamics simulation, namely the first-order, the second-order, and the scheme derived through implementation of the Verlet discretisation, which all showed a second-order accuracy both in spatial and time coordinates with respect to the convective system. They argued that such equivalence breaks down when the nature of the physical systems necessitates the inclusion of external forcing expression.

Silva and Semiao [7] carried out a comprehensive assessment of distinct lattice Boltzmann remarks using Chapman-Enskog analysis. Guo et al. [8] highlight the significance of the different lattice Boltzmann schemes towards the accuracy of the recovered Navier-Stokes expression from the Chapman-Enskog analysis. Additionally, they mentioned that the choice of discrete forcing model depends heavily upon the exactitude of the restored continuum hydrodynamics representation.

On the other hand, the discrete forcing model in LBM is the other prominent property when modelling the flow is sought. Several authors have proposed diverse expressions to accommodate external forcing term in the generic lattice Boltzmann equation. Luo [9] was among the first authors to propose a mathematical expression for the discrete forcing term in LBM, alongside with He et al. [10] and Guo et al. [8,11]. Later on, Kupershtokh et al. [12] introduced a forcing model based on the association of exact-difference-method upon the corresponding Boltzmann equation.

The presence of different mathematical expressions for both the discrete lattice Boltzmann equation and the forcing model offers diverse LBM strategies for hydrodynamics modelling. However, choosing a suitable approach is still a matter of debate. To alleviate such issues, Mohamad and Kuzmin [13] investigated the behaviour of three different forcing models by simulating natural convection in closed and open-ended cavities. They found that the investigated forcing models produced equivalent numerical solutions at steady-state conditions.

Subsequently, Krivovichev [14] presented a comprehensive evaluation regarding stability analysis of the six widely-used forcing models based on the application of the von Neumann method to linear approximation of the system of nonlinear lattice Boltzmann expressions. They found that better stability properties prevailed upon the forcing models that are implicit in their nature. Zheng et al. [15] found that as long as the simulation comprises low Mach number flow, different forcing schemes in LBM would return equivalent steady-state solutions.

It is apparent from the available literature that few works have looked into the implications of both distinct lattice Boltzmann expressions and different forcing models in LBM simulation. Moreover, the primary focus of the published works has revolved around the discrepancy in the computational characteristics of distinct LBM scenarios during the steady-state condition of the simulation, leaving the behaviour during the unsteady period of the flow unexplained. Therefore, the present work aims to expand the evaluation of the capacity of disparate LBM schemes by incorporating the variety in both the discrete lattice Boltzmann expressions and the discrete forcing models into the workflow of the assessment. Emphasis was given upon revealing the computational characteristic of distinct LBM scenarios during the unsteady-period of the simulation. The steady-state solutions were considered for the exhibition and validation purposes.

In this study, two different embodiments of discrete Boltzmann expression and three distinct forcing models were incorporated into the analysis. For the sake of providing comprehensive evaluation, the capacity of disparate LBM schemes was tested upon simulating two non-isothermal thermo-hydrodynamics systems, namely natural convection in a differentially-heated cavity and Rayleigh-Bénard convection.

The current research article is organized as follows. Section 2 presents the foundational aspect of natural convection and heat transfer arrangement. Section 3 describes the distinct LBM strategies for simulating the concomitant physical phenomena. Section 4 deals with

theoretical outlook of disparate LBM scenarios, while the results of numerical testing are discussed in Section 5. Some concluding remarks are posed in Section 6.

2. Governing Mathematical Remarks and Principal Dimensionless Groups

Natural convection phenomena is governed by two flowing materials that propagate simultaneously and synergistically within the flow domain, namely the fluid and thermal substances. Accordingly, the natural convection is governed by three fundamental equations, namely, the continuity, Navier-Stokes, and heat equations [16], expressed as

$$\frac{\partial \rho}{\partial t} + \frac{\partial}{\partial x_\alpha}(\rho u_\alpha) = 0 \tag{1}$$

$$\frac{\partial}{\partial t}(\rho u_\alpha) + \frac{\partial}{\partial x_\beta}(\rho u_\alpha u_\beta) = -\frac{\partial p}{\partial x_\beta} + \mu \frac{\partial}{\partial x_\beta} \left(\frac{\partial u_\alpha}{\partial x_\beta} + \frac{\partial u_\beta}{\partial x_\alpha} \right) + F_\alpha \tag{2}$$

$$\frac{\partial T}{\partial t} + \frac{\partial}{\partial x_\alpha}(T u_\alpha) = \frac{\partial}{\partial x_\alpha} \left(D \frac{\partial T}{\partial x_\alpha} \right), \tag{3}$$

where ρ , u_i , p , T , μ and D denote the fluid density, velocity, pressure, temperature, dynamic viscosity, and thermal diffusion coefficient, respectively. The contribution from the buoyancy effect was designated by F_α .

In the present work, the natural convection was examined under the Boussinesq approximation [13,17]. As such, it neglected the contributions to the dynamical behaviour of the flowing substances from viscous heat dissipation and compression caused. Therefore, the buoyancy term occupies the following definition [13]:

$$F_\alpha = \rho G_\alpha \beta_T (T - T_{\text{ref}}), \tag{4}$$

where G_α specifies the gravitational acceleration, β_T depicts the thermal expansion coefficient, and T_{ref} represents the assigned reference temperature.

It is customary within CFD to express the associated physical quantities using non-dimensional units. For natural convection phenomena, the key dimensionless groups were identified as follows:

$$Nu = \frac{hL}{\rho D c_p}; \quad Pr = \frac{v}{D}; \quad Ra = \frac{G_y \beta_T (T_{\text{hot}} - T_{\text{cold}}) L^3}{v D}, \tag{5}$$

where Nu , Pr , and Ra designate the Nusselt, Prandtl, and Rayleigh number, accordingly. T_{hot} and T_{cold} denote the hot and cold temperature conditions, respectively. Physical quantities of h , c_p , and L represent, respectively, the heat transfer coefficient, fluid specific heat capacity, and the characteristic length of the domain.

Furthermore, the present work uses the following generic dimensionless expressions to designate the horizontal and vertical length of the flow domain.

$$x^* = \frac{x}{L}; \quad y^* = \frac{y}{L}; \quad u_\alpha^* = \frac{u_\alpha L}{D}. \tag{6}$$

In Equation (6), x and y express, respectively, the horizontal and vertical length of the investigated domain.

3. Lattice Boltzmann Expressions from Distinct Truncation Order

In the present work, consideration was given to the double-distribution-function (DDF) approach to establish a proper representation of the dynamical entities [17]. This would mean that the prevalence of two continuous Boltzmann expressions, which should be discretised either by capturing only the first-truncation order or considering up to the second-truncation term of the expanded-Boltzmann equation. Regardless the approach considered, different representations of the discrete lattice Boltzmann equation are obtained.

For the fluid component, the first- and second-order discrete lattice Bhatnagar-Gross-Krook (BGK) equations are expressed as follows:

$$f_i(x_\alpha + \xi_{i\alpha}\Delta t, t + \Delta t) - f_i(x_\alpha, t) = -\frac{\Delta t}{\tau_v} \left(f_i(x_\alpha, t) - f_i^{eq}(x_\alpha, t) \right) + R_i(x_\alpha, t)\Delta t \quad (7)$$

$$\bar{f}_i(x_\alpha + \xi_{i\alpha}\Delta t, t + \Delta t) - \bar{f}_i(x_\alpha, t) = -\frac{\Delta t}{\bar{\tau}_v} \left(\bar{f}_i(x_\alpha, t) - f_i^{eq}(x_\alpha, t) \right) + R_i(x_\alpha, t)\Delta t \left(1 - \frac{\Delta t}{2\bar{\tau}_v} \right), \quad (8)$$

where f_i indicates the discrete fluid populations, $\xi_{i\alpha}$ specifies the discrete velocity of fluid particles, R_i designates the discrete form of the external force term, τ_v denotes the relaxation time for fluid particles, and Δt specifies the discrete time step.

For the second-order lattice BGK model, the corresponding discrete fluid population \bar{f}_i and its corresponding relaxation time $\bar{\tau}_v$ were defined accordingly as in [6,10]:

$$\bar{f}_i = f_i + \frac{\Delta t}{2\tau_v} \left(f_i - f_i^{eq} \right) - \frac{R_i\Delta t}{2} \quad (9)$$

$$\bar{\tau}_v = \tau_v + \frac{\Delta t}{2}, \quad (10)$$

where f_i^{eq} depicts the equilibrium condition of the fluid population.

The equilibrium distribution function f_i^{eq} occupies the following remark:

$$f_i^{eq} = \rho w_i \left(1 + \frac{\xi_{i\alpha} u_\alpha}{c_s^2} + \frac{(\xi_{i\alpha} u_\alpha)^2}{2c_s^4} - \frac{u_\alpha u_\beta}{2c_s^2} \right), \quad (11)$$

where c_s designates the lattice speed of sound and w_i represents the discrete weighting coefficient.

In the present work, the D2Q9 velocity arrangement was selected to model fluid displacements. Such configuration satisfies the following descriptions:

$$\xi_{i\alpha} = \begin{cases} (0, 0), & \text{for } i = 0 \\ (1, 0), (0, 1), (-1, 0), (0, -1), & \text{for } i = 1, 2, 3, 4 \\ (1, 1), (-1, 1), (-1, -1), (1, -1), & \text{for } i = 5, 6, 7, 8 \end{cases} \quad (12)$$

$$w_i = \begin{cases} \frac{4}{9}, & \text{for } i = 0 \\ \frac{1}{9}, & \text{for } i = 1, 2, 3, 4 \\ \frac{1}{36}, & \text{for } i = 5, 6, 7, 8. \end{cases} \quad (13)$$

Apart from the dichotomy in the lattice BGK representation for fluid movements, the discrete manifestation of forcing term R_i also occupies diverse expressions. In this study, three of the most prominent R_i models were selected for the evaluation, namely the scheme proposed by Luo [9], Guo et al. [8], and Kupershtokh et al. [12], expressed respectively as follows:

$$R_i = w_i \frac{\xi_{i\alpha} F_\alpha}{c_s^2} \quad (14)$$

$$R_i = w_i \left(\frac{\xi_{i\alpha} - u_\alpha}{c_s^2} + \frac{(\xi_{i\alpha} u_\alpha) \xi_{i\alpha}}{c_s^4} \right) F_\alpha \quad (15)$$

$$R_i = f_i^{eq}(\rho, u_\alpha + \Delta u_\alpha) - f_i^{eq}(\rho, u_\alpha). \quad (16)$$

For the thermal constituent, due to the absence of external force term, the discretisation operation of Boltzmann representation of thermal substance is not affected by the selected truncation order. Therefore, the lattice BGK formula representing the thermal dissemination only occupies a single mathematical expression, namely,

$$g_i(x_\alpha + e_{i\alpha}\Delta t, t + \Delta t) - g_i(x_\alpha, t) = -\frac{\Delta t}{\tau_D} \left(g_i(x_\alpha, t) - g_i^{eq}(x_\alpha, t) \right), \quad (17)$$

where g_i identifies the discrete thermal population, $e_{i\alpha}$ denotes the discrete velocity of thermal particles, and τ_D designates the relaxation time for thermal elements.

The associated thermal equilibrium population g_i^{eq} was defined as follows:

$$g_i^{eq} = z_i T \left(1 + \frac{e_{i\alpha} u_\alpha}{c_s^2} + \frac{(e_{i\alpha} u_\alpha)^2}{2c_s^4} - \frac{u_\alpha u_\beta}{2c_s^2} \right). \tag{18}$$

For thermal dissemination, D2Q5 discrete velocity set was adopted. Implementation of fewer velocity directions to represent thermal displacements was possible due to the lower isotropy nature pertinent to thermal populations in the corresponding lattice Boltzmann arrangement. As can be seen in Appendix B, the associated Chapman-Enskog analysis of thermal particles only necessitates low-order moment expansion terms in order to recover correct macroscopic heat formulation. Consequently, the isotropy requirement for thermal displacement modelling in LBM can be conducted properly by fewer lattice arrangement, such as the D2Q5 velocity set [2].

For the adopted D2Q5 configuration, the discrete velocity of thermal particles $e_{i\alpha}$ and their corresponding weighting factor z_i adhere to the following descriptions:

$$e_{i\alpha} = \begin{cases} (0, 0), & \text{for } i = 0 \\ (1, 0), (0, 1), (-1, 0), (0, -1), & \text{for } i = 1, 2, 3, 4 \end{cases} \tag{19}$$

$$z_i = \begin{cases} \frac{2}{6}, & \text{for } i = 0 \\ \frac{1}{6}, & \text{for } i = 1, 2, 3, 4. \end{cases} \tag{20}$$

At this point, it is apparent that there exist distinct strategies to administer natural convection and heat transfer modelling with LBM.

Table 1 outlines the plausible LBM scenarios considered in the present work, as well as the corresponding scheme.

Table 1. The plausible arrangements for simulating the buoyancy-driven natural convection flow with lattice Boltzmann method.

LBM Scheme	Lattice BGK Model for Fluid Displacement	Discrete Forcing Model
IA	First-Order	Luo [9] (Equation (14))
IB	Lattice BGK Model	Guo et al. [8] (Equation (15))
IC	(Equation (7))	Kupershtokh et al. [12] (Equation (16))
IIA	Second-Order	Luo [9] (Equation (14))
IIB	Lattice BGK Model	Guo et al. [8] (Equation (15))
IIC	(Equation (8))	Kupershtokh et al. [12] (Equation (16))

4. Recovery of the Macroscopic Thermo-Hydrodynamics Expressions from Disparate LBM Arrangements in Natural Convection Heat Transfer Modelling

As a thermo-hydrodynamics solver, LBM is closely tied to the macroscopic heat and mass transport formulations. It is therefore pivotal to uncover the capacity of each considered LBM schemes in returning the fundamental macroscopic relationships. This objective was fulfilled through evaluating the Chapman-Enskog analysis [7,8,18]. Appendices A and B provide the details of undertaken procedures for the associated fluid and thermal components, respectively.

From the corresponding Chapman-Enskog analysis, the restored macroscopic equations of mass, momentum, and heat transport were captured as follows:

$$\frac{\partial \rho}{\partial t} + \frac{\partial}{\partial x_\alpha} (\rho u_\alpha) = \frac{\partial}{\partial x_\alpha} \left(F_\alpha \left(m \Delta t - \frac{m(\Delta t)^2}{2\sigma} - \frac{\Delta t}{2} \varphi \right) \right) \tag{21}$$

$$\begin{aligned} \frac{\partial}{\partial t}(\rho u_\alpha) + \frac{\partial}{\partial x_\beta}(\rho u_\alpha u_\beta) = & -\frac{\partial}{\partial x_\beta}(\rho c_s^2 \delta_{\alpha\beta}) + \rho c_s^2 \left(\sigma - \frac{\Delta t}{2}\right) \frac{\partial}{\partial x_\beta} \left(\frac{\partial u_\alpha}{\partial x_\beta} + \frac{\partial u_\beta}{\partial x_\alpha}\right) \\ & + \left(\varphi + \frac{m\Delta t}{\sigma}\right) F_\alpha + \frac{\partial}{\partial t} \left(F_\alpha \left(m\Delta t - \frac{m(\Delta t)^2}{2\sigma} - \frac{\Delta t}{2}\varphi\right)\right) \\ & + \left(\sigma - \frac{\Delta t}{2}\right) \left(\varphi + \frac{m\Delta t}{\sigma}\right) \frac{\partial}{\partial x_\beta} (u_\alpha F_\beta + F_\alpha u_\beta) \\ & - \left(\sigma - \frac{\Delta t}{2}\right) \frac{\partial}{\partial x_\beta} \frac{\partial}{\partial x_\gamma} (\rho u_\alpha u_\beta u_\gamma) - \sigma \varphi \frac{\partial}{\partial x_\beta} \sum_i \xi_{i\alpha} \xi_{i\beta} R_i. \end{aligned} \tag{22}$$

$$\frac{\partial T}{\partial t} + \frac{\partial}{\partial x_\alpha}(Tu_\alpha) = \frac{\partial}{\partial x_\alpha} \left(c_s^2 \left(\tau_D - \frac{\Delta t}{2}\right) \frac{\partial T}{\partial x_\alpha}\right) + \left(\tau_D - \frac{\Delta t}{2}\right) \frac{\partial}{\partial x_\alpha} \left(T \left(\frac{\partial u_\alpha}{\partial t} + \frac{\partial}{\partial x_\beta} (u_\alpha u_\beta)\right)\right). \tag{23}$$

In Equation (22), the term $\sum_i \xi_{i\alpha} \xi_{i\beta} R_i$ specifies the second-order moment of the forcing term. Details regarding the mathematical expressions of all the associated forcing moments are appended in Appendix A of this manuscript. In Equations (21) and (22), quantities m , σ , and φ occupy the following definitions:

$$m = \begin{cases} 0, & \text{for scenario IA, IB and IC} \\ \frac{1}{2}, & \text{for scenario IIA, IIB and IIC} \end{cases} \tag{24}$$

$$\sigma = \begin{cases} \tau_v, & \text{for scenario IA, IB and IC} \\ \bar{\tau}_v, & \text{for scenario IIA, IIB and IIC} \end{cases} \tag{25}$$

$$\varphi = \begin{cases} 1, & \text{for scenario IA, IB and IC} \\ \left(1 - \frac{\Delta t}{2\bar{\tau}_v}\right), & \text{for scenario IIA, IIB and IIC.} \end{cases} \tag{26}$$

From the recovered thermo-hydrodynamics expressions of Equations (21)–(23), it was observed that each of the corresponding LBM scenarios returns the macroscopic hydrodynamics relationships with residual fractions. Such properties occupy different mathematical expressions depending upon the selected LBM scenarios. Table 2 summarizes the corresponding mathematical remarks of hydrodynamics residual fractions from distinct LBM schemes. On the other hand, the restored heat formulation of Equation (23) contains only one residual fraction, appropriately depicted by the last term on the right hand side of the formula. Nevertheless, it is important to mention that the particular thermal residual fraction incorporates momentum terms from the fluid constituents within its expression.

Table 2. The captured residual fractions in the recovered continuity and Navier-Stokes equations from every considered LBM scenarios.

LBM Scheme	Residual Fractions in the Restored Continuity Equation	Residual Fractions in the Restored Navier-Stokes Equation
IA	$-\frac{\Delta t}{2} \frac{\partial F_\alpha}{\partial x_\alpha}$	$-\frac{\Delta t}{2} \frac{\partial F_\alpha}{\partial t} + \left(\tau_v - \frac{\Delta t}{2}\right) \frac{\partial}{\partial x_\beta} (u_\alpha F_\beta + F_\alpha u_\beta)$
IB	$-\frac{\Delta t}{2} \frac{\partial F_\alpha}{\partial x_\alpha}$	$-\frac{\Delta t}{2} \frac{\partial F_\alpha}{\partial t} - \frac{\Delta t}{2} \frac{\partial}{\partial x_\beta} (u_\alpha F_\beta + F_\alpha u_\beta)$
IC	$-\frac{\Delta t}{2} \frac{\partial F_\alpha}{\partial x_\alpha}$	$-\frac{\Delta t}{2} \frac{\partial F_\alpha}{\partial t} - \frac{\Delta t}{2} \frac{\partial}{\partial x_\beta} (u_\alpha F_\beta + F_\alpha u_\beta) - \tau_v \frac{\partial}{\partial x_\beta} \left(\frac{F_\alpha F_\beta}{\rho}\right)$
IIA	0	$\left(\bar{\tau}_v - \frac{\Delta t}{2}\right) \frac{\partial}{\partial x_\beta} (u_\alpha F_\beta + F_\alpha u_\beta)$
IIB	0	0
IIC	0	$-\left(\bar{\tau}_v - \frac{\Delta t}{2}\right) \frac{\partial}{\partial x_\beta} \left(\frac{F_\alpha F_\beta}{\rho}\right)$

Consequently, the residual term in the recovered heat equation is linked indirectly to the residual terms in the restored Navier-Stokes formula of Equation (22).

5. Numerical Results and Discussions

To test the computational performance of disparate LBM scenarios, two distinctive thermo-hydrodynamics flow systems (the natural convection in a differentially-heated

cavity and the Rayleigh-Bénard convection) were selected. The simulations of both physical phenomena were performed in a two-dimensional close system under the condition of $Ra = 10^4$ and $Pr = 0.71$. The computational workloads were administered upon the graphical processing unit (GPU) ecosystem so as to expedite the analyses. In such physical arrangements, the Mach number (Ma) was defined as

$$Ma = \frac{u_{char}}{c_s} = \sqrt{\frac{Ra v^2}{Pr H^2 c_s^2}} \tag{27}$$

where u_{char} designates the characteristic velocity of the flowing material.

The particular property was defined as

$$u_{char} = \sqrt{G_y \beta_T (\Theta_{hot} - \Theta_{cold}) H} = \sqrt{\frac{Ra v^2}{Pr H^2}} \tag{28}$$

where Θ_{hot} and Θ_{cold} specify, respectively, the dimensionless hot and cold temperatures. In general, the dimensionless temperature is expressed as

$$\Theta = \frac{T - T_{ref}}{T_{hot} - T_{cold}} \tag{29}$$

where T_{ref} denotes the reference temperature.

The expressions for fluid kinematic viscosity ν and thermal diffusivity D were obtained, respectively, as

$$\nu = \begin{cases} c_s^2 \left(\tau_v - \frac{\Delta t}{2} \right), & \text{for scenario IA, IB and IC} \\ c_s^2 \left(\bar{\tau}_v - \frac{\Delta t}{2} \right), & \text{for scenario IIA, IIB and IIC} \end{cases} \tag{30}$$

$$D = c_s^2 \left(\tau_D - \frac{\Delta t}{2} \right). \tag{31}$$

5.1. Simulation of Natural Convection in a Differentially-Heated Cavity

Figure 1 schematized the physical configuration of natural convection in a differentially-heated enclosure.

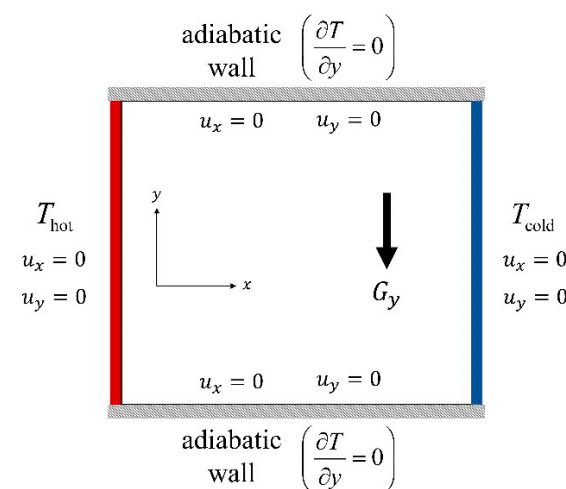


Figure 1. Domain configuration for two-dimensional natural convection in a differentially-heated cavity.

The entire domain was assumed filled with an inert fluid. The vertical walls of the cavity were characterised by contrasting thermal conditions. The left-border was consid-

ered hot (T_{hot}) while the opposite wall was assumed cold (T_{cold}). On the other hand, the horizontal boundaries were set to be perfectly insulated. For the fluid substance, the non-equilibrium bounce-back (NEBB) technique [19] was adopted upon all the corresponding perimeters, including the four corners. The NEBB method defines the unknown fluid populations at the boundaries from the known populations by evaluating the non-equilibrium condition of the normal populations at local boundary sites.

The non-equilibrium condition at the boundary wall satisfies the following remark:

$$\zeta_{\bar{i}} - f_{\bar{i}}^{eq} = \zeta_i - f_i^{eq} - \zeta_{i\alpha} N_\alpha, \tag{32}$$

where N_α notifies the momentum correction factor due to inclusion of the external forcing term into the generic Boltzmann expression of the fluid populations. The subscript symbol \bar{i} specifies the opposite direction of i . Parameter ζ_i was defined as follows:

$$\zeta_i = \begin{cases} f_{i'} & \text{for scenario IA, IB and IC} \\ \bar{f}_{i'} & \text{for scenario IIA, IIB and IIC.} \end{cases} \tag{33}$$

Meanwhile, for the thermal population, the anti-bounce-back (ABB) [2] and central finite difference [20] strategies were administered upon the vertical and horizontal boundaries, respectively.

ABB technique was administered by adopting the following relationship for the associated boundary walls:

$$g_{\bar{i}}(x_{boundary}, t + \Delta t) = -g_i^*(x_{boundary}, t) + 2z_i T_{wall}, \tag{34}$$

where g_i^* depicts thermal populations after collision and T_{wall} notifies the prescribed temperature condition at particular boundary wall. To accomplish a valid comparison, numerical simulations for all the considered LBM scenarios were accomplished under similar hydrodynamic relaxation time ($\tau_v = 0.6$) and Mach number ($Ma = 0.1$) conditions.

Thereupon, the average Nusselt number $\langle Nu \rangle$ was appointed as the dimensionless property that represents the heat transfer performance of each concomitant LBM scheme. This property abides to the following description:

$$\langle Nu \rangle = 1 + \left(\frac{\langle u_x^* \Theta \rangle}{\Theta_{hot} - \Theta_{cold}} \right), \tag{35}$$

where $\langle u_x^* \Theta \rangle$ represents the average of the product between the dimensionless horizontal velocity and the dimensionless temperature over the entire simulation domain. For the sake of validation, the associated steady-state flow profile from scenario IIB was selected as the representation to exhibit the final streamlines and isotherms from the corresponding heat and mass transport system.

Figure 2 exhibits the steady-state streamlines and isotherms from the selected LBM scenario. The corresponding streamlines and isotherms profiles demonstrate an excellent agreement with the literature [16,17,21,22]. It was found, however, that the results from the six associated LBM scenarios exhibit almost similar steady-state flow profiles. Therefore, every considered LBM scheme possesses similar qualification in delivering legitimate steady-state numerical solutions.

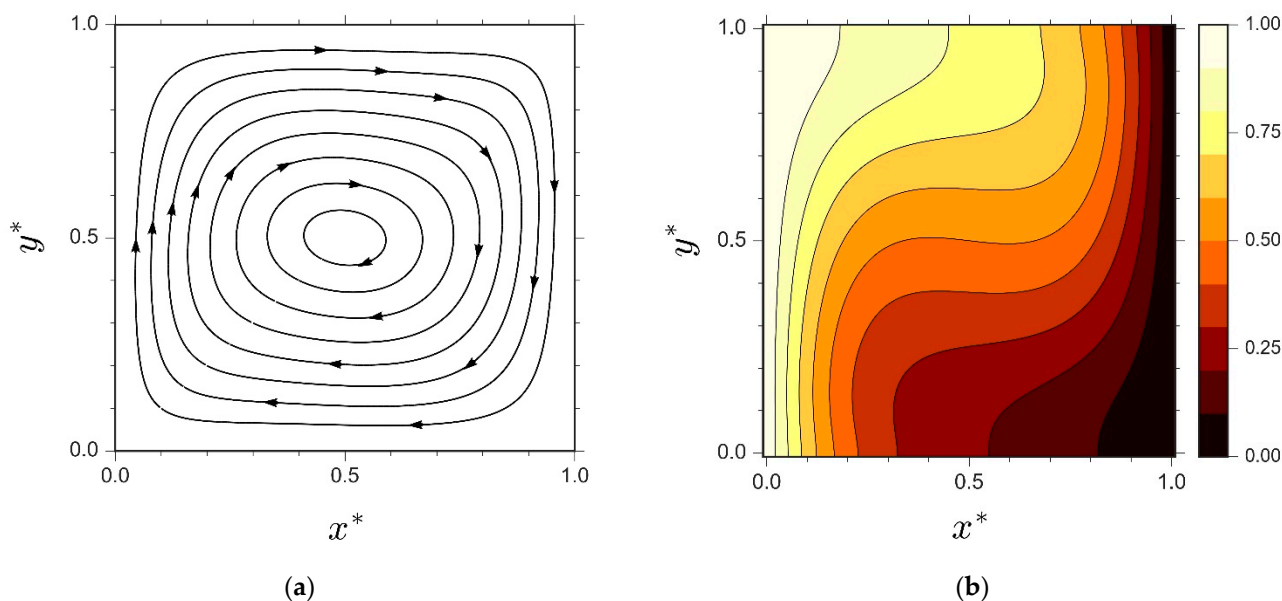


Figure 2. Steady-state flow characteristics of two-dimensional natural convection in a differentially-heated cavity for $Ra = 10^4$, $Pr = 0.71$, $\tau_v = 0.6$ and $Ma = 0.1$ from scenario IIB, displaying (a) Streamlines and (b) Isotherms contour.

Table 3 outlines the principal steady-state numerical properties from distinct LBM schemes. The parameters were compared with the outcomes of finite difference method (FDM) [23] and finite element method (FEM) [24]. A closer look on Table 3 reveals that LBM scenarios, which adopt a second-order lattice BGK model (i.e., scenario IIA, IIB, and IIC) were capable of delivering better compliance with the benchmark solutions than the ones which comprise first-order lattice BGK scheme (i.e., scenario IA, IB, and IC).

Table 3. Steady-state properties of two-dimensional natural convection in a differentially-heated cavity for $Ra = 10^4$, $Pr = 0.71$, $\tau_v = 0.6$, and $Ma = 0.1$, compared with solutions of finite difference method (FDM) [23] and finite element method (FEM) [24].

Simulation Parameters	LBM Scheme (Present Study)						FDM [23]	FEM [24]
	IA	IB	IC	IIA	IIB	IIC		
$\langle Nu \rangle$	2.2341	2.2339	2.2339	2.2424	2.2423	2.2424	2.243	2.2448
Max $u_x^* \dagger$	16.0678	16.0619	16.0619	16.1742	16.1732	16.1742	16.178	16.1853
Max $u_y^* \ddagger$	19.3927	19.3864	19.3864	19.6011	19.5999	19.6011	19.617	19.6316
Location of Max $u_x^* \dagger$	0.8116	0.8116	0.8116	0.8204	0.8204	0.8204	0.823	0.8230
Location of Max $u_y^* \ddagger$	0.1159	0.1159	0.1159	0.1189	0.1189	0.1189	0.119	0.1188

\dagger at $x^* = 0.5$; \ddagger at $y^* = 0.5$.

Undoubtedly, the inclusion of higher-truncation order terms empowers the second-order lattice BGK scheme with superior numerical accuracy to the corresponding first-order counterpart. Contrastingly, trivial disparity in computing performance was observed upon implementation of different forcing models.

Recording the behaviour of specific parameters along the simulation process provides a way of uncovering additional key information regarding the computational capacity of the considered LBM schemes. Figure 3a shows the profiles of $\langle Nu \rangle$ from different LBM scenarios with the dimensional simulation time t appointed as the horizontal axis. Figure 3b illustrates similar profiles with dimensionless simulation time t^* used as the corresponding horizontal axis. Both figures display the existence of striking contrast in the computational characteristics among distinct LBM scenarios.

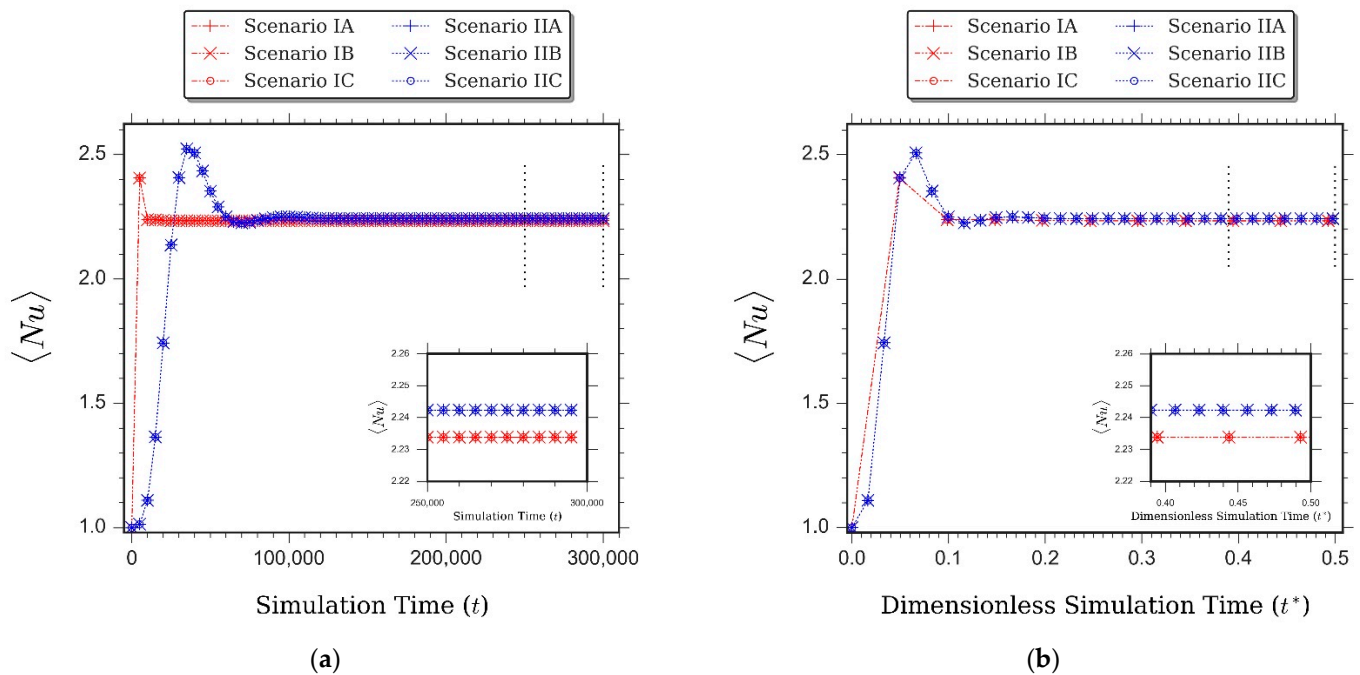


Figure 3. Profiles of average Nusselt number $\langle Nu \rangle$ from different LBM scenarios during the unsteady period up to the accomplishment of the steady-state condition of the natural convection in a differentially-heated cavity for $Ra = 10^4$, $Pr = 0.71$, $\tau_v = 0.6$, and $Ma = 0.1$, showing computational behaviour with (a) dimensional simulation time t as the horizontal axis, and (b) dimensionless simulation time t^* as the horizontal axis. Figure insets demonstrate the magnification of the computational characteristics in the steady-state region of the simulation.

As depicted in Figure 3a, the discrepancy was predominantly apparent when the simulations were performed in an unsteady-state period fashion. Altering the fashion from unsteady to steady state, the disparity either decreases gradually or was negligible (Figure 3a). Such discrepancy was in agreement with the physical properties outlined Table 3.

Figure 3a unveils essential information regarding the primary factors responsible for the observed discrepancy in computational performance of distinct LBM scenarios. It appears then that the different order of lattice BGK expression is the predominant factor that generates the observed disparity in computational characteristics of different LBM schemes. On the other hand, the contribution of distinct forcing strategies upon such disparity was found to be inconsequential. Figure 3a reveals further that LBM schemes, which administer second-order lattice BGK model (i.e., scenarios IIA, IIB, and IIC) exhibited slower progression towards steady-state condition than those schemes which implement first-order lattice BGK model (i.e., scenarios IA, IB, and IC).

However, when non-dimensional time t^* was assimilated, the slower progression characteristic of the second-order schemes vanished. Figure 3b shows that the computational performance of the second-order lattice BGK schemes is proportional to the first-order scenarios. The profiles of dimensionless horizontal velocity u_x^* at the vertical mid-plane of the enclosure ($x^* = 0.5$) were displayed in Figure 4. Therein, the profiles of u_x^* demonstrate similar behaviour with the ones observed in Figure 3a.

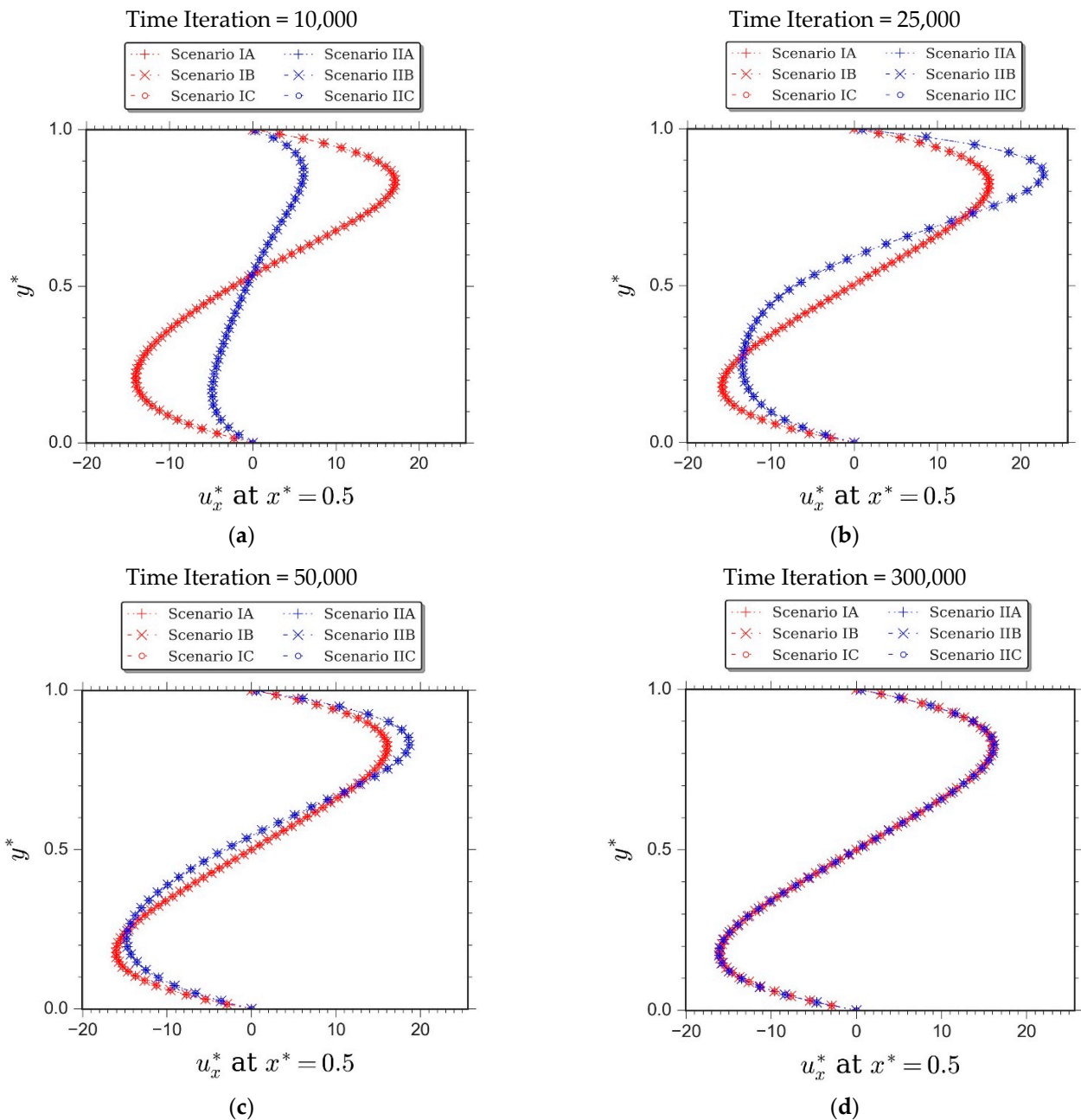


Figure 4. Profiles of dimensionless horizontal velocity at the vertical mid-plane of the cavity upon different simulation periods of natural convection in differentially-heated cavity for $Ra = 10^4$, $Pr = 0.71$, $\tau_v = 0.6$ and $Ma = 0.1$, demonstrating condition at time iteration: (a) 10,000; (b) 25,000; (c) 50,000 and (d) 300,000.

Figure 5 displays the corresponding computational overhead from every considered LBM scenario. The scenario IIC was identified as the particular LBM scheme with the highest computational demand in modelling fluid flow and heat transfer in a differentially-heated cavity, therein.

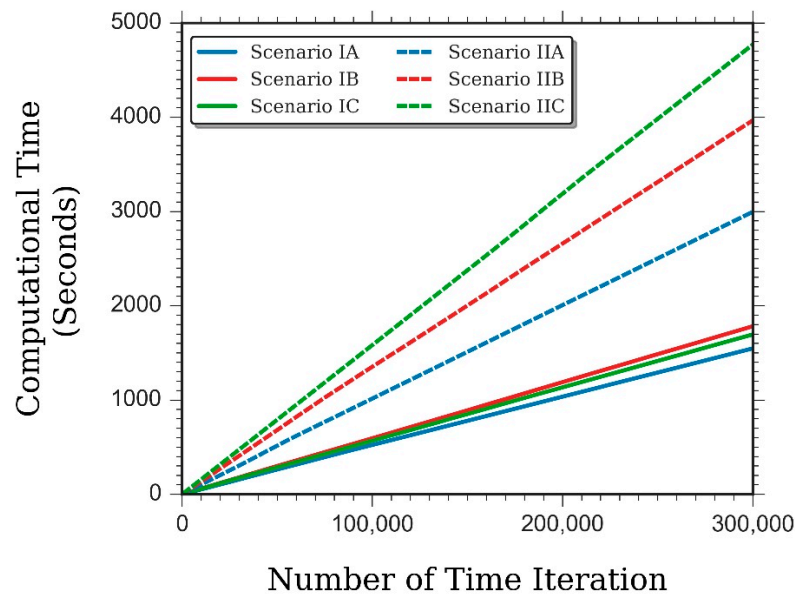


Figure 5. Computational overhead of disparate LBM schemes in modelling natural convection in a differentially-heated cavity with $Ra = 10^4$, $Pr = 0.71$, $\tau_v = 0.6$ and $Ma = 0.1$, starting from the unsteady period up to the accomplishment of the steady-state period.

5.2. Simulation of Rayleigh-Bénard Convection

After undertaking evaluation regarding computational characteristics of distinct LBM scenarios upon simulating natural convection in a differentially-heated enclosure in the previous section, the current segment of the article aims at elucidating the capacity of disparate LBM scenarios while simulating the Rayleigh-Bénard convection (RBC) phenomena as illustrated in Figure 6.

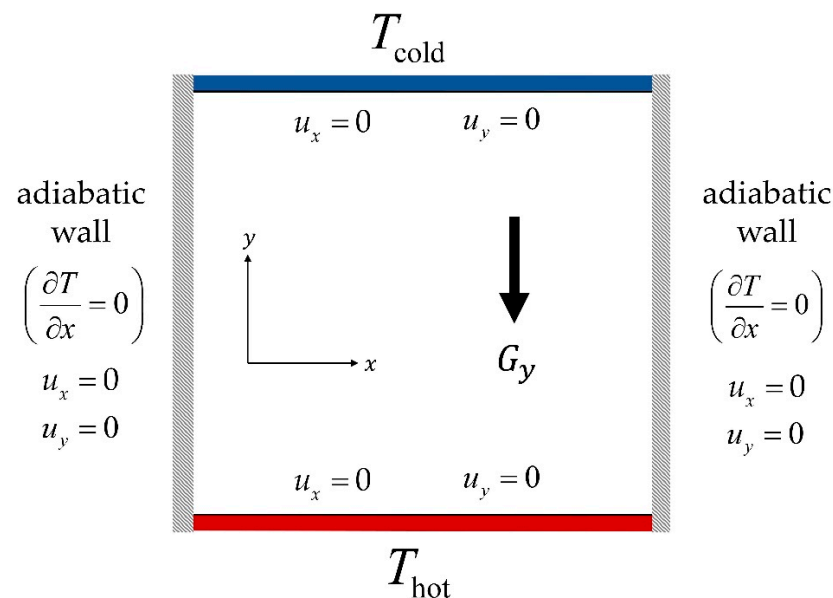


Figure 6. Domain configuration for two-dimensional Rayleigh-Bénard convection with aspect ratio one.

Hot temperature conditions were imposed upon the horizontal bottom wall while the opposing top margin was set to occupy cold temperature. The vertical boundaries were set to be perfectly insulated. Boundary treatments were accomplished through adopting similar strategies with the erstwhile case of natural convection in a differentially-heated

cavity. However, appropriate adjustments were necessary in order to account the appointed wall conditions in RBC configuration.

The contrasting driving force from buoyancy and gravitational attraction in the RBC system results in perpetual competition between the tendency of the flowing materials to move upward and downward, correspondingly. Such a situation enables the associated thermo-hydrodynamics phenomena to exhibit a number of plausibly distinct flow behaviours with variable convection roll patterns [25,26]. To mitigate such complexity, the present study assimilates infinitesimal disturbances into the corresponding physical system. These perturbation functions are described as

$$\Theta_{\text{initial}}(x, y) = \Theta_{\text{hot}} - \left(\frac{(\Theta_{\text{hot}} - \Theta_{\text{cold}})y}{N_y} \left(1 - 0.001 \sin\left(\frac{2\pi x}{N_x}\right) \right) \right) \tag{36}$$

$$\rho_{\text{initial}}(x, y) = \rho_{\text{ref}} \left(1 + \beta_T \frac{(\Theta_{\text{hot}} - \Theta_{\text{cold}})y}{N_y} \left(1 - 0.001 \sin\left(\frac{2\pi x}{N_x}\right) \right) \right), \tag{37}$$

where N_x and N_y designate the associated lattice nodes in the horizontal and vertical directions of the spatial coordinate, respectively.

The performance of heat transfer in RBC system was represented by the average Nusselt number at the hot wall, $\langle Nu \rangle_0$. The corresponding parameter was mathematically expressed as

$$\langle Nu \rangle_0 = \frac{1}{N_x(\Theta_{\text{hot}} - \Theta_{\text{cold}})} \sum_{i=1}^{N_x} q_y(i)|_{y=0}. \tag{38}$$

Here, q_y specifies the local heat flux in vertical direction, defined as

$$q_y = u_y^* \Theta - \frac{\partial \Theta}{\partial y}. \tag{39}$$

The last term on the right-hand side of the above formula denotes temperature gradient in a vertical direction.

Figure 7 presents the final streamlines and isotherms for RBC simulation with $Ra = 10^4$ and $Pr = 0.71$. Similar to the former case of natural convection in a differentially-heated cavity, the steady-state flow profile from scenario IIB was selected for exhibition and validation purposes. The corresponding streamlines and isotherms displayed in Figure 7 were in excellent agreement with the earlier work of Ouertatani et al. [27]. Similarly to the former case of natural convection in a differentially-heated cavity, the obtained steady-state responses from distinct LBM schemes demonstrate identical flow profiles.

Nevertheless, minor discrepancy was observed in the captured $\langle Nu \rangle_0$ solutions, which are summarized and compared with the outcomes of finite volume method (FVM) [27] in Table 4.

Table 4. Average Nusselt number at the hot wall $\langle Nu \rangle_0$ of the Rayleigh-Bènard convection system from distinct LBM schemes during the steady-state period of the flow for aspect ratio = 1, $Ra = 10^4$, $Pr = 0.71$, $\tau_v = 0.6$, and $Ma = 0.1$ compared with the outcome of the finite volume method (FVM) [27].

Simulation Parameter	LBM Scheme (Present Study)						FVM [27]
	IA	IB	IC	IIA	IIB	IIC	
$\langle Nu \rangle_0$	2.1681	2.1684	2.1684	2.1554	2.1555	2.1554	2.1581

A better accuracy of $\langle Nu \rangle_0$ solutions was obtained from the LBM scenarios which adopt a second-order lattice BGK model. The profiles of $\langle Nu \rangle_0$ along the simulation process exhibited characteristics similar to those observed in the former natural convection case. Figure 8a illustrates further the behaviour of $\langle Nu \rangle_0$. A slow progression characteristic of the second-order lattice BGK schemes was observed that disappears as the horizontal axis

is replaced by the associated dimensionless simulation time t^* . Figure 9 shows the profiles of dimensionless vertical velocity u_y^* at the horizontal mid-plane of the cavity ($y^* = 0.5$). Therein, similar computational behaviour was observed as the one prevailing in Figure 8a.

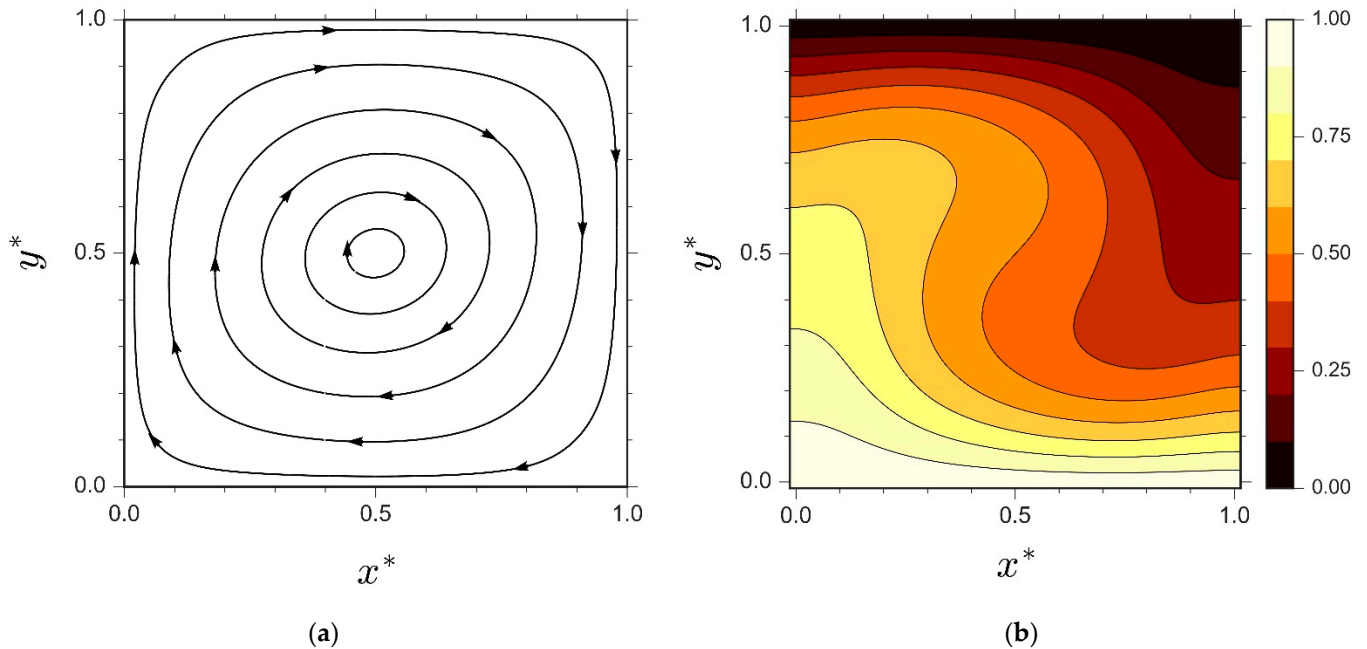


Figure 7. Steady-state flow characteristics of Rayleigh-Bénard convection with aspect ratio = 1, $Ra = 10^4$, $Pr = 0.71$, $\tau_v = 0.6$, and $Ma = 0.1$ from scenario IIB, displaying (a) Streamlines and (b) Isotherms contour.

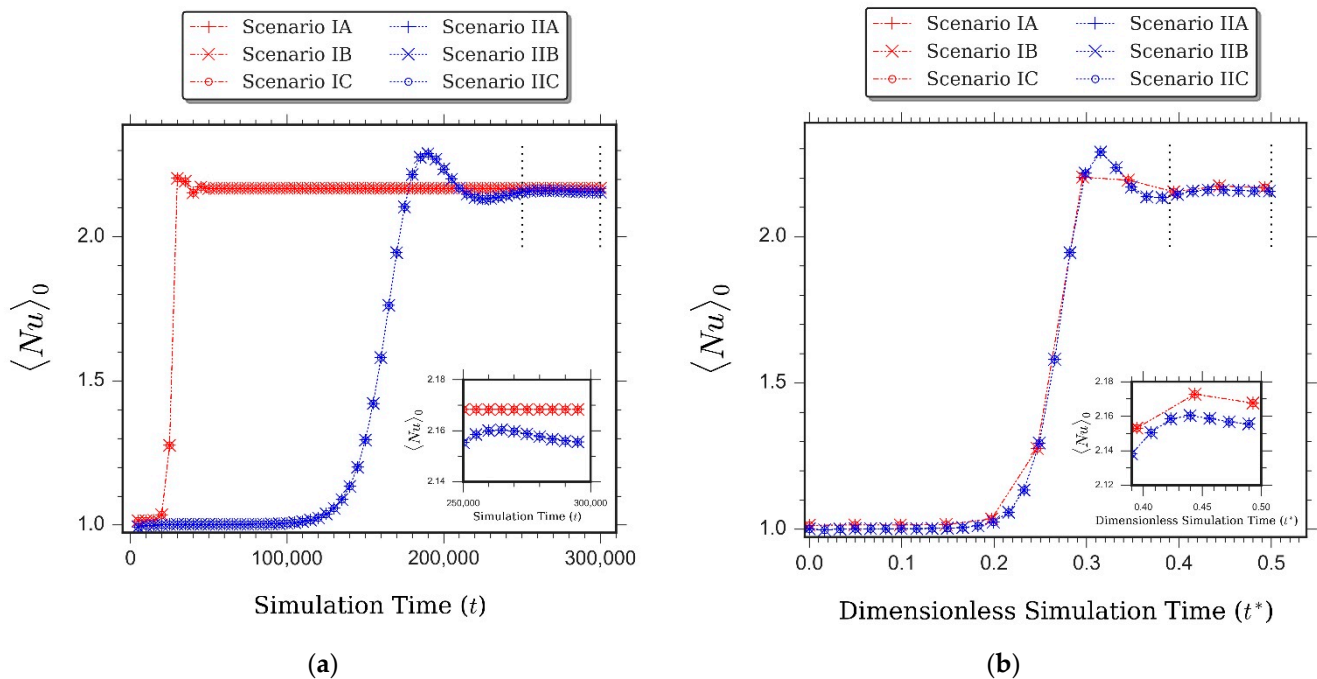


Figure 8. Profiles of average Nusselt number at the hot wall $\langle Nu \rangle_0$ from different LBM scenarios during the unsteady period up to the accomplishment of steady-state condition of the Rayleigh-Bénard convection for aspect ratio = 1, $Ra = 10^4$, $Pr = 0.71$, $\tau_v = 0.6$, and $Ma = 0.1$, showing computational behaviour with (a) dimensional simulation time t as the horizontal axis and (b) dimensionless simulation time t^* as the horizontal axis. Figure insets display the magnification of the computational characteristics in the steady-state region of the simulation.

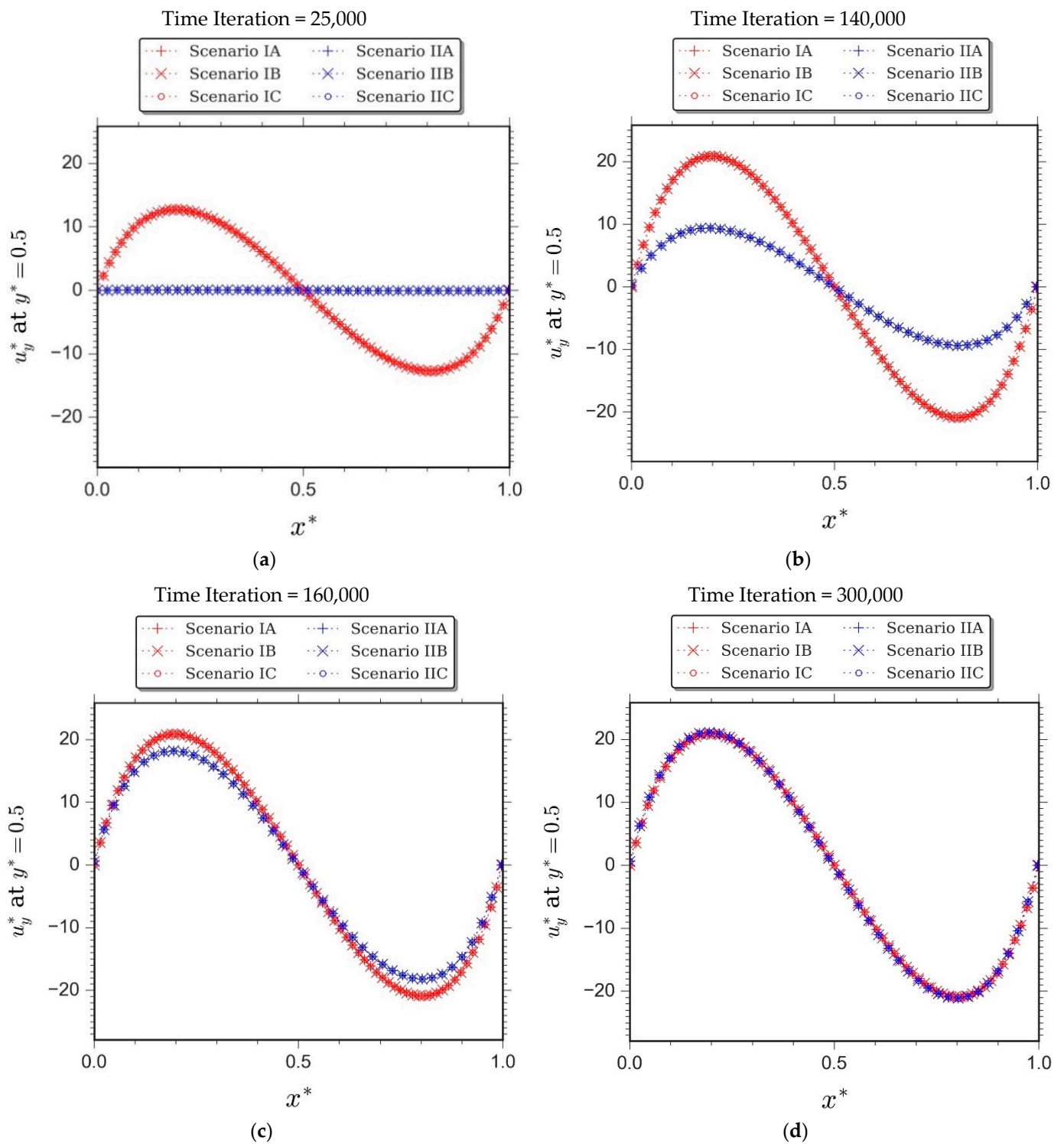


Figure 9. Profiles of dimensionless vertical velocity at the horizontal mid-plane of the cavity upon different simulation periods of Rayleigh–Bénard convection for aspect ratio = 1, $Ra = 10^4$, $Pr = 0.71$, $\tau_v = 0.6$, and $Ma = 0.1$, demonstrating conditions at the following time iterations: (a) 25,000; (b) 140,000; (c) 160,000; and (d) 300,000.

Figure 10 depicts the corresponding profiles of computational cost from every considered LBM schemes. Similar with the case of natural convection in a differentially-heated cavity, higher computational demand was displayed by the LBM schemes which adopt a second-order lattice BGK model.

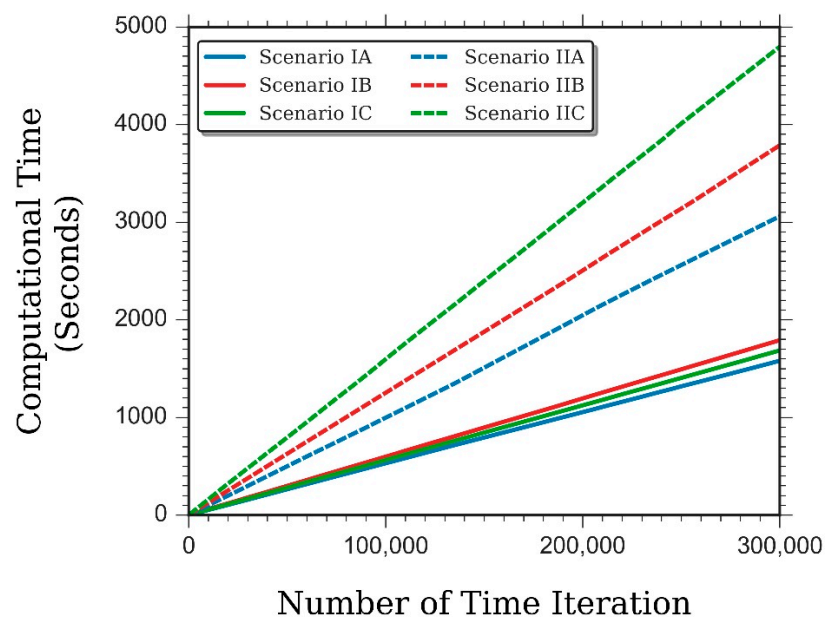


Figure 10. Computational overhead of disparate LBM schemes in modelling Rayleigh-Bénard convection with aspect ratio = 1, $Ra = 10^4$, $Pr = 0.71$, $\tau_v = 0.6$ and $Ma = 0.1$, starting from the transient period up to the accomplishment of the quasi-steady-state period.

6. Conclusions

Comprehensive evaluation regarding the efficacy of disparate Lattice Boltzmann Method (LBM) scenarios upon simulation of fluid flow and heat transfer phenomena were studied. The primary objective, herein addressed, was the evaluation of the plausible discrepancy in the computational characteristics of different LBM scenarios when simulating natural convection and heat transfer systems during the unsteady period of the flow. To fulfil the sought objective, the LBM schemes were tested upon two distinctive thermo-hydrodynamics systems, namely the natural convection in a differentially-heated cavity and the Rayleigh-Bénard convection. The key findings of this work are as follows:

- 1 The presence of considerable discrepancy in computational characteristics of disparate LBM schemes was seen during the unsteady period of the simulation, which diminished gradually as the simulation advanced towards a steady-state condition.
- 2 Variation in the associated discrete lattice Boltzmann expression was identified as the predominant factor inherent to discrepancy in computational characteristics.
- 3 The contribution of distinct forcing models upon the heterogeneity in computational behaviour was found to be trivial.
- 4 At a steady-state condition, the LBM schemes which administer a second-order lattice BGK model recovered better numerical accuracy than those scenarios which comprise a first-order lattice BGK model. However, the scheme is challenged by higher computational demand.

Author Contributions: A.D.H. devised the numerical methodology, conceptualisation, and composition of the present study, as well as developing the computer codes and preparing the original manuscript. K.S. contributes upon conceptualisation, supervision, reviewing, and editing the manuscript. Y.S. and R.N. provide supervision as well as editing the original manuscript. All authors have read and agreed to the published version of the manuscript.

Funding: This research received no external funding.

Data Availability Statement: This research does not accommodate data sharing option.

Acknowledgments: A.D.H. thanks the Japanese Ministry of Education, Culture, Sports, Science and Technology (MEXT) for bestowing financial support upon his doctoral training. The authors

are indebted to Fajril Ambia of SKK Migas, Indonesia, for his auspicious suggestions during the development of computer codes of this study.

Conflicts of Interest: The authors declare no conflict of interest.

Nomenclature

ρ	fluid density, kg/m ³ ;	x_α	spatial coordinates vector
T	temperature, K;	u_α	fluid velocity, m/s
μ	Fluid dynamic viscosity; kg/m · s	F_α	external force, N
ν	fluid kinematic viscosity, m ² /s;	G_α	gravity acceleration, m/s ²
D	thermal diffusivity, m ² /s;	β_T	thermal expansion coefficient, K ⁻¹
T_{ref}	reference temperature, K	c_s	lattice speed of sound
T_{hot}	hot temperature, K;	u_{char}	characteristic velocity
T_{cold}	cold temperature, K;	Nu	Nusselt number, dimensionless
h	heat transfer coefficient, W/m ² · K;	$\langle Nu \rangle$	average Nusselt number for the entire simulation domain
c_p	specific heat capacity, J/kg · K;	$\langle Nu \rangle_0$	average Nusselt number at the hot wall
L	characteristic length, m;	Pr	Prandtl number, dimensionless
Δt	simulation time step, lattice unit;	Ra	Rayleigh number, dimensionless
f_i	fluid population;	Ma	Mach number, dimensionless
f_i^{eq}	equilibrium fluid population;	x^*	dimensionless horizontal length
g_i	thermal population;	y^*	dimensionless vertical length
g_i^{eq}	equilibrium thermal population;	u_α^*	dimensionless fluid velocity
R_i	discrete forcing term;	N_x	number of lattice nodes in the horizontal direction
w_i	weighting coefficients for fluid population;	N_y	number of lattice nodes in the vertical direction
z_i	weighting coefficients for thermal population;	q_y	local heat flux;
<i>Greek symbols</i>			
$\xi_{i\alpha}$	discrete velocity for fluid particles;	τ_v	relaxation time for fluid population
$e_{i\alpha}$	discrete velocity for thermal particles;	τ_D	relaxation time for thermal population
Θ	dimensionless temperature;	δ_{ij}	delta Kronecker
Θ_{hot}	dimensionless hot temperature;	ϵ	Knudsen number, dimensionless
Θ_{cold}	dimensionless cold temperature;		
<i>Subscript</i>			
i	number of discrete velocities		
α, β, γ	direction of spatial coordinates (Einstein notation).		

Appendix A. The Chapman-Enskog Analysis for Fluid Populations

The Chapman-Enskog analysis was commenced by defining the following expanded fractions:

$$\begin{aligned} \zeta_i &= f_i^{eq} + \epsilon \zeta_i^{(1)} + \epsilon^2 \zeta_i^{(2)} \\ \frac{\partial}{\partial t} &= \epsilon \frac{\partial}{\partial t_1} + \epsilon^2 \frac{\partial}{\partial t_2} \\ \zeta_{i\alpha} \frac{\partial}{\partial x_\alpha} &= \epsilon \zeta_{i\alpha} \frac{\partial}{\partial x_\alpha^{(1)}} + \epsilon^2 \zeta_{i\alpha} \frac{\partial}{\partial x_\alpha^{(2)}} \\ R_i &= \epsilon R_i^{(1)}. \end{aligned} \tag{A1}$$

In the above relationships, ϵ denotes small quantity which value lies within the order of Knudsen number and ζ_i satisfies the remark described in Equation (33).

Adopting Taylor series expansion upon the generalized lattice Boltzmann expression for fluid components around equilibrium condition by taking ϵ as the expansion quantity returns the mathematical expressions for the first- and second-order expansion terms of the fluid density evolution equation, correspondingly depicted as

$$\begin{aligned} O(\epsilon) : \left(\frac{\partial}{\partial t_1} + \zeta_{i\alpha} \frac{\partial}{\partial x_\alpha^{(1)}} \right) f_i^{eq} &= -\frac{1}{\sigma} \zeta_i^{(1)} + \varphi R_i^{(1)} \\ O(\epsilon^2) : \left(\frac{\partial}{\partial t_2} + \zeta_{i\alpha} \frac{\partial}{\partial x_\alpha^{(2)}} \right) f_i^{eq} &+ \left(\frac{\partial}{\partial t_1} + \zeta_{i\alpha} \frac{\partial}{\partial x_\alpha^{(1)}} \right) \left(\left(1 - \frac{\Delta t}{2\sigma} \right) \zeta_i^{(1)} + \frac{\Delta t}{2} \varphi R_i^{(1)} \right) = -\frac{1}{\sigma} \zeta_i^{(2)}, \end{aligned} \tag{A2}$$

where $O(\epsilon)$ and $O(\epsilon^2)$ specify respectively the first- and second-order expansion terms of the fluid density evolution equation. Parameters σ and φ occupy similar definitions as those provided in Equations (25) and (26), respectively.

Thereupon, expressions of moments of $O(\epsilon)$ and $O(\epsilon^2)$ can be obtained as follows:
 Moments of $O(\epsilon)$:

$$\begin{aligned} \sum_i \left(\frac{\partial}{\partial t_1} + \xi_{i\alpha} \frac{\partial}{\partial x_\alpha^{(1)}} \right) f_i^{eq} &= \sum_i \left(-\frac{1}{\sigma} \zeta_i^{(1)} + \varphi R_i^{(1)} \right) \\ \sum_i \xi_{i\alpha} \left(\frac{\partial}{\partial t_1} + \xi_{i\alpha} \frac{\partial}{\partial x_\alpha^{(1)}} \right) f_i^{eq} &= \sum_i \xi_{i\alpha} \left(-\frac{1}{\sigma} \zeta_i^{(1)} + \varphi R_i^{(1)} \right) \\ \sum_i \xi_{i\alpha} \xi_{i\beta} \left(\frac{\partial}{\partial t_1} + \xi_{i\alpha} \frac{\partial}{\partial x_\alpha^{(1)}} \right) f_i^{eq} &= \sum_i \xi_{i\alpha} \xi_{i\beta} \left(-\frac{1}{\sigma} \zeta_i^{(1)} + \varphi R_i^{(1)} \right) \end{aligned} \tag{A3}$$

Moments of $O(\epsilon^2)$:

$$\begin{aligned} \sum_i \left(\frac{\partial}{\partial t_2} + \xi_{i\alpha} \frac{\partial}{\partial x_\alpha^{(2)}} \right) f_i^{eq} + \sum_i \left(\frac{\partial}{\partial t_1} + \xi_{i\alpha} \frac{\partial}{\partial x_\alpha^{(1)}} \right) \left(1 - \frac{\Delta t}{2\sigma} \right) \zeta_i^{(1)} \\ + \sum_i \left(\frac{\partial}{\partial t_1} + \xi_{i\alpha} \frac{\partial}{\partial x_\alpha^{(1)}} \right) \frac{\Delta t}{2} \varphi R_i^{(1)} = -\frac{1}{\sigma} \sum_i \zeta_i^{(2)} \\ \sum_i \xi_{i\alpha} \left(\frac{\partial}{\partial t_2} + \xi_{i\alpha} \frac{\partial}{\partial x_\alpha^{(2)}} \right) f_i^{eq} + \sum_i \xi_{i\alpha} \left(\frac{\partial}{\partial t_1} + \xi_{i\alpha} \frac{\partial}{\partial x_\alpha^{(1)}} \right) \left(1 - \frac{\Delta t}{2\sigma} \right) \zeta_i^{(1)} \\ + \sum_i \xi_{i\alpha} \left(\frac{\partial}{\partial t_1} + \xi_{i\alpha} \frac{\partial}{\partial x_\alpha^{(1)}} \right) \frac{\Delta t}{2} \varphi R_i^{(1)} = -\frac{1}{\sigma} \sum_i \xi_{i\alpha} \zeta_i^{(2)}. \end{aligned} \tag{A4}$$

Subsequently, the expressions for the three particular moments, namely the moments of the discrete forcing terms R_i , the moments of the equilibrium density population f_i^{eq} and the moments of the expanded population ζ_i have to be configured. Table A1 summarizes the expressions of forcing moments.

Table A1. Mathematical expressions for the moments of the discrete forcing terms R_i for the three considered forcing schemes.

Forcing Model	Zereth-Order Moment ($\sum_i R_i$)	First-Order Moment ($\sum_i \xi_{i\alpha} R_i$)	Second-Order Moment ($\sum_i \xi_{i\alpha} \xi_{i\beta} R_i$)
Luo (Equation (14))	0	F_α	0
Guo, et al. (Equation (15))	0	F_α	$F_\alpha u_\beta + u_\alpha F_\beta$
Kupershtokh, et al. (Equation (16))	0	F_α	$F_\alpha u_\beta + u_\alpha F_\beta + \frac{1}{\rho} (F_\alpha F_\beta)$

The expressions for the moments of f_i^{eq} and ζ_i were obtained accordingly as:
 Moments of f_i^{eq} :

$$\begin{aligned} \sum_i f_i^{eq} &= \sum_i \zeta_i + m\Delta t \sum_i R_i = \rho \\ \sum_i \xi_{i\alpha} f_i^{eq} &= \sum_i \xi_{i\alpha} \zeta_i + m\Delta t \sum_i \xi_{i\alpha} R_i = \rho u_\alpha \\ \sum_i \xi_{i\alpha} \xi_{i\beta} f_i^{eq} &= \sum_i \xi_{i\alpha} \xi_{i\beta} \zeta_i + m\Delta t \sum_i \xi_{i\alpha} \xi_{i\beta} R_i = \rho u_\alpha u_\beta + \rho c_s^2 \delta_{\alpha\beta} \\ \sum_i \xi_{i\alpha} \xi_{i\beta} \xi_{i\gamma} f_i^{eq} &= \sum_i \xi_{i\alpha} \xi_{i\beta} \xi_{i\gamma} \zeta_i + m\Delta t \sum_i \xi_{i\alpha} \xi_{i\beta} \xi_{i\gamma} R_i = \rho c_s^2 (u_\alpha \delta_{\beta\gamma} + u_\beta \delta_{\alpha\gamma} + u_\gamma \delta_{\alpha\beta}) \end{aligned} \tag{A5}$$

Moments of ζ_i :

$$\begin{aligned} \sum_i \zeta_i^{(1)} &= -m\Delta t \sum_i R_i^{(1)}; & \sum_i \zeta_i^{(2)} &= 0 \\ \sum_i \xi_{i\alpha} \zeta_i^{(1)} &= -m\Delta t \sum_i \xi_{i\alpha} R_i^{(1)}; & \sum_i \xi_{i\alpha} \zeta_i^{(2)} &= 0 \\ \sum_i \xi_{i\alpha} \xi_{i\beta} \zeta_i^{(1)} &= -m\Delta t \sum_i \xi_{i\alpha} \xi_{i\beta} R_i^{(1)}; & \sum_i \xi_{i\alpha} \xi_{i\beta} \zeta_i^{(2)} &= 0 \\ \sum_i \xi_{i\alpha} \xi_{i\beta} \xi_{i\gamma} \zeta_i^{(1)} &= -m\Delta t \sum_i \xi_{i\alpha} \xi_{i\beta} \xi_{i\gamma} R_i^{(1)}; & \sum_i \xi_{i\alpha} \xi_{i\beta} \xi_{i\gamma} \zeta_i^{(2)} &= 0. \end{aligned} \tag{A6}$$

Substituting the expressions of R_i , f_i^{eq} and ζ_i moments into Equations (A3) and (A4), the following remarks emerged:

$$\frac{\partial \rho}{\partial t_1} + \frac{\partial}{\partial x_\alpha^{(1)}}(\rho u_\alpha) = 0 \tag{A7}$$

$$\frac{\partial}{\partial t_1}(\rho u_\alpha) + \frac{\partial}{\partial x_\beta^{(1)}}(\rho u_\alpha u_\beta + \rho c_s^2 \delta_{\alpha\beta}) = \left(\varphi + \frac{m\Delta t}{\sigma}\right) \sum_i \zeta_{i\alpha} R_i^{(1)} \tag{A8}$$

$$\begin{aligned} \frac{\partial}{\partial t_1}(\rho u_\alpha u_\beta + \rho c_s^2 \delta_{\alpha\beta}) = & -\frac{\partial}{\partial x_\gamma^{(1)}}(\rho c_s^2 u_\alpha \delta_{\beta\gamma} + \rho c_s^2 u_\beta \delta_{\alpha\gamma} + \rho c_s^2 u_\gamma \delta_{\alpha\beta}) \\ & + \left(\varphi + \frac{m\Delta t}{\sigma}\right) \sum_i \zeta_{i\alpha} \zeta_{i\beta} R_i^{(1)} \end{aligned} \tag{A9}$$

$$\begin{aligned} \frac{\partial \rho}{\partial t_2} + \frac{\partial}{\partial x_\alpha^{(2)}}(\rho u_\alpha) = & \frac{\partial}{\partial t_1} \sum_i R_i^{(1)} \left(m\Delta t - \frac{m(\Delta t)^2}{2\sigma} - \frac{\Delta t}{2} \varphi\right) \\ & + \frac{\partial}{\partial x_\alpha^{(1)}} \sum_i \zeta_{i\alpha} R_i^{(1)} \left(m\Delta t - \frac{m(\Delta t)^2}{2\sigma} - \frac{\Delta t}{2} \varphi\right) \end{aligned} \tag{A10}$$

$$\begin{aligned} \frac{\partial}{\partial t_2}(\rho u_\alpha) + \frac{\partial}{\partial x_\beta^{(2)}}(\rho u_\alpha u_\beta + \rho c_s^2 \delta_{\alpha\beta}) = & \frac{\partial}{\partial t_1} \sum_i \zeta_{i\alpha} R_i^{(1)} \left(m\Delta t - \frac{m(\Delta t)^2}{2\sigma} - \frac{\Delta t}{2} \varphi\right) \\ & + \frac{\partial}{\partial x_\beta^{(1)}} \sum_i \zeta_{i\alpha} \zeta_{i\beta} R_i^{(1)} \left(m\Delta t - \frac{m(\Delta t)^2}{2\sigma} - \frac{\Delta t}{2} \varphi\right), \end{aligned} \tag{A11}$$

where m occupies similar description as the one presented in Equation (24). Combining Equations (A7)–(A11) as well as substituting expressions of forcing moments from Table A1, the macroscopic hydrodynamics relationships of Equations (21) and (22) were restored. The residual fractions prevailed in the recovered hydrodynamics equations from each considered LBM scenarios were summarized in Table 2.

Appendix B. The Chapman-Enskog Analysis for Thermal Populations

For the thermal populations, the Chapman-Enskog analysis was performed following similar fashion as in the preceding analysis for the fluid components. However, the discrete velocity of thermal particles $e_{i\alpha}$ was used instead of velocity of fluid particles $\zeta_{i\alpha}$. The expanded terms for the thermal population occupy the following descriptions:

$$\begin{aligned} g_i &= g_i^{eq} + \epsilon g_i^{(1)} + \epsilon^2 g_i^{(2)} \\ \frac{\partial}{\partial t} &= \epsilon \frac{\partial}{\partial t_1} + \epsilon^2 \frac{\partial}{\partial t_2} \\ e_{i\alpha} \frac{\partial}{\partial x_\alpha} &= \epsilon e_{i\alpha} \frac{\partial}{\partial x_\alpha^{(1)}} + \epsilon^2 e_{i\alpha} \frac{\partial}{\partial x_\alpha^{(2)}}. \end{aligned} \tag{A12}$$

Executing similar fashion of Taylor series expansion upon the generalized lattice Boltzmann expression for the thermal particles produces the corresponding remarks:

$$\begin{aligned} O(\epsilon) : & \left(\frac{\partial}{\partial t_1} + e_{i\alpha} \frac{\partial}{\partial x_\alpha^{(1)}}\right) g_i^{eq} = -\frac{1}{\tau_D} g_i^{(1)} \\ O(\epsilon^2) : & \left(\frac{\partial}{\partial t_2} + e_{i\alpha} \frac{\partial}{\partial x_\alpha^{(2)}}\right) g_i^{eq} + \left(\frac{\partial}{\partial t_1} + e_{i\alpha} \frac{\partial}{\partial x_\alpha^{(1)}}\right) \left(1 - \frac{\Delta t}{2\tau_D}\right) g_i^{(1)} = -\frac{1}{\tau_D} g_i^{(2)}. \end{aligned} \tag{A13}$$

The corresponding moments of $O(\epsilon)$ and $O(\epsilon^2)$ terms can be configured as follows: Moments of $O(\epsilon)$:

$$\begin{aligned} \sum_i \left(\frac{\partial}{\partial t_1} + e_{i\alpha} \frac{\partial}{\partial x_\alpha^{(1)}}\right) g_i^{eq} &= \sum_i \left(-\frac{1}{\tau_D} g_i^{(1)}\right) \\ \sum_i e_{i\alpha} \left(\frac{\partial}{\partial t_1} + e_{i\alpha} \frac{\partial}{\partial x_\alpha^{(1)}}\right) g_i^{eq} &= \sum_i e_{i\alpha} \left(-\frac{1}{\tau_D} g_i^{(1)}\right) \end{aligned} \tag{A14}$$

Moments of $O(\epsilon^2)$:

$$\sum_i \left(\frac{\partial}{\partial t_2} + e_{i\alpha} \frac{\partial}{\partial x_\alpha^{(2)}} \right) g_i^{eq} + \sum_i \left(\frac{\partial}{\partial t_1} + e_{i\alpha} \frac{\partial}{\partial x_\alpha^{(1)}} \right) \left(1 - \frac{\Delta t}{2\tau_D} \right) g_i^{(1)} = \sum_i \left(-\frac{1}{\tau_D} g_i^{(2)} \right). \quad (A15)$$

The moments of the thermal equilibrium population g_i^{eq} occupy the following definitions:

$$\begin{aligned} \sum_i g_i^{eq} &= T \\ \sum_i e_{i\alpha} g_i^{eq} &= Tu_\alpha \\ \sum_i e_{i\alpha} e_{i\beta} g_i^{eq} &= Tc_s^2 \delta_{\alpha\beta} + Tu_\alpha u_\beta. \end{aligned} \quad (A16)$$

Substituting Formula (A16) into Equations (A14) and (A15), the following expressions prevailed:

$$\frac{\partial T}{\partial t_1} + \frac{\partial}{\partial x_\alpha^{(1)}} (Tu_\alpha) = 0 \quad (A17)$$

$$\begin{aligned} \frac{\partial T}{\partial t_2} + \frac{\partial}{\partial x_\alpha^{(2)}} (Tu_\alpha) &= c_s^2 \left(\tau_D - \frac{\Delta t}{2} \right) \left(\frac{\partial}{\partial x_\alpha^{(1)}} \frac{\partial}{\partial x_\alpha^{(1)}} (T) + \frac{1}{c_s^2} \frac{\partial}{\partial t_1} \frac{\partial}{\partial x_\alpha^{(1)}} (Tu_\alpha) \right) \\ &+ \left(\tau_D - \frac{\Delta t}{2} \right) \frac{\partial}{\partial x_\alpha^{(1)}} \frac{\partial}{\partial x_\beta^{(1)}} (Tu_\alpha u_\beta). \end{aligned} \quad (A18)$$

Combining Equations (A17) and (A18), the macroscopic heat equation depicted by Equation (23) was recovered.

References

1. He, X.; Doolen, G.D. Thermodynamic foundations of kinetic theory and lattice Boltzmann models for multiphase flows. *J. Stat. Phys.* **2002**, *107*, 309–328. [\[CrossRef\]](#)
2. Kruger, T.; Kusumaatmaja, H.; Kuzmin, A.; Shardt, O.; Goncalo, S.; Viggien, E.M. *The Lattice Boltzmann Method, Principles and Practice*; Springer: Cham, Switzerland, 2017; ISBN 9783319446479.
3. Trouette, B. Lattice Boltzmann simulations of a time-dependent natural convection problem. *Comput. Math. Appl.* **2013**, *66*, 1360–1371. [\[CrossRef\]](#)
4. Mezrhab, A.; Amine Moussaoui, M.; Jami, M.; Naji, H.; Bouzidi, M. Double MRT thermal lattice Boltzmann method for simulating convective flows. *Phys. Lett. Sect. A Gen. Solid State Phys.* **2010**, *374*, 3499–3507. [\[CrossRef\]](#)
5. Jami, M.; Moufekkir, F.; Mezrhab, A.; Fontaine, J.P.; Bouzidi, M. New thermal MRT lattice Boltzmann method for simulations of convective flows. *Int. J. Sci.* **2016**, *100*, 98–107. [\[CrossRef\]](#)
6. Ubertini, S.; Asinari, P.; Succi, S. Three ways to lattice Boltzmann: A unified time-marching picture. *Phys. Rev. E-Stat. Nonlinear Soft Matter Phys.* **2010**, *81*, 1–11. [\[CrossRef\]](#)
7. Silva, G.; Semiao, V. First and Second-order forcing expressions in a lattice Boltzmann method reproducing isothermal hydrodynamics in artificial compressibility form. *J. Fluid Mech.* **2012**, *698*, 282–303. [\[CrossRef\]](#)
8. Guo, Z.; Zheng, C.; Shi, B. Discrete lattice effects on the forcing term in the lattice Boltzmann method. *Phys. Rev. E-Stat. Phys. Plasmas Fluids Relat. Interdiscip. Top.* **2002**, *65*, 6. [\[CrossRef\]](#)
9. Luo, L.S. Theory of the lattice Boltzmann method: Lattice Boltzmann models for nonideal gases. *Phys. Rev. E-Stat. Phys. Plasmas Fluids Relat. Interdiscip. Top.* **2000**, *62*, 4982–4996. [\[CrossRef\]](#) [\[PubMed\]](#)
10. He, X.; Chen, S.; Doolen, G.D. A novel thermal model for the lattice Boltzmann method in incompressible limit. *J. Comput. Phys.* **1998**, *146*, 282–300. [\[CrossRef\]](#)
11. Guo, Z.; Zhao, T.S. Lattice Boltzmann model for incompressible flows through porous media. *Phys. Rev. E-Stat. Phys. Plasmas Fluids Relat. Interdiscip. Top.* **2002**, *66*, 1–9. [\[CrossRef\]](#) [\[PubMed\]](#)
12. Kupershtokh, A.L.; Medvedev, D.A.; Karpov, D.I. On equations of state in a lattice Boltzmann method. *Comput. Math. Appl.* **2009**, *58*, 965–974. [\[CrossRef\]](#)
13. Mohamad, A.A.; Kuzmin, A.A. Critical evaluation of force term in lattice Boltzmann method, natural convection problem. *Int. J. Heat Mass Transf.* **2010**, *53*, 990–996. [\[CrossRef\]](#)
14. Krivovichev, G.V. Stability analysis of body force action models used in the single-relaxation-time single-phase lattice Boltzmann method. *Appl. Math. Comput.* **2019**, *348*, 25–41. [\[CrossRef\]](#)
15. Zheng, L.; Zheng, S.; Zhai, Q. Analysis of force treatment in lattice Boltzmann equation method. *Int. J. Heat Mass Transf.* **2019**, *139*, 747–750. [\[CrossRef\]](#)
16. Mayne, D.A.; Usmani, A.S.; Crapper, M. H-adaptive finite element solution of high Rayleigh number thermally driven cavity problem. *Int. J. Numer. Methods Heat Fluid Flow* **2000**, *10*, 598–615. [\[CrossRef\]](#)

17. Du, R.; Liu, W. A new multiple-relaxation-time lattice Boltzmann method for natural convection. *J. Sci. Comput.* **2013**, *56*, 122–130. [[CrossRef](#)]
18. He, X.; Luo, L.S. Theory of the lattice Boltzmann method: From the Boltzmann equation to the lattice Boltzmann equation. *Phys. Rev. E-Stat. Phys. Plasmas Fluids Relat. Interdiscip. Top.* **1997**, *55*, 6811–6820. [[CrossRef](#)]
19. Zou, Q.; He, X. On pressure and velocity boundary conditions for the lattice Boltzmann BGK model. *Phys. Fluids* **1997**, *9*, 1591–1596. [[CrossRef](#)]
20. Shu, C.; Peng, Y.; Chew, Y.T. Simulation of natural convection in a square cavity by Taylor series expansion and least squares-based lattice Boltzmann method. *Int. J. Mod. Phys. C* **2002**, *13*, 1399–1414. [[CrossRef](#)]
21. Dixit, H.N.; Babu, V. Simulation of high Rayleigh number natural convection in a square cavity using the lattice Boltzmann method. *Int. J. Heat Mass Transf.* **2006**, *49*, 727–739. [[CrossRef](#)]
22. Yu, P.X.; Tian, Z.F. Compact computations based on a stream-function-velocity formulation of two-dimensional steady laminar natural convection in a square cavity. *Phys. Rev. E-Stat. Nonlinear Soft Matter Phys.* **2012**, *85*, 1–12. [[CrossRef](#)] [[PubMed](#)]
23. De Vahl Davis, G. Natural convection of air in a square cavity: A bench mark numerical solution. *Int. J. Numer. Methods Fluids* **1983**, *3*, 249–264. [[CrossRef](#)]
24. Syrjälä, S. Higher order penalty-galerkin finite element approach to laminar natural convection in a square cavity. *Numer. Heat Transf. Part A Appl.* **1996**, *29*, 197–210. [[CrossRef](#)]
25. Goldhirsch, I.; Pelz, R.B.; Orszag, S.A. Numerical simulation of thermal convection in a two-dimensional finite box. *J. Fluid Mech.* **1989**, *199*, 1–28. [[CrossRef](#)]
26. Shan, X. Simulation of Rayleigh-Bénard convection using a lattice Boltzmann method. *Phys. Rev. E-Stat. Phys. Plasmas Fluids Relat. Interdiscip. Top.* **1997**, *55*, 2780–2788. [[CrossRef](#)]
27. Ouertatani, N.; Ben Cheikh, N.; Ben Beya, B.; Lili, T. Numerical simulation of two-dimensional Rayleigh-Bénard convection in an enclosure. *Comptes Rendus Mécanique* **2008**, *336*, 464–470. [[CrossRef](#)]